

## WEAK SINDY: GALERKIN-BASED DATA-DRIVEN MODEL SELECTION

DANIEL A. MESSENGER AND DAVID M. BORTZ

**ABSTRACT.** We present a novel weak formulation and discretization for discovering general equations from noisy measurement data. This method of learning differential equations from data fits into a new class of algorithms that replace pointwise derivative approximations with linear transformations and a variance reduction techniques. Our approach improves on the standard SINDy algorithm presented in [4] by orders of magnitude. We first show that in the noise-free regime, this so-called Weak SINDy (WSINDy) framework is capable of recovering the dynamic coefficients to very high accuracy, with the number of significant digits equal to the tolerance of the data simulation scheme. Next we show that the weak form naturally accounts for white noise by identifying the correct nonlinearities with coefficient error scaling favorably with the signal-to-noise ratio while significantly reducing the size of linear systems in the algorithm. In doing so, we combine the ease of implementation of the SINDy algorithm with the natural noise-reduction of integration as demonstrated in [12] to arrive at a more robust and practical method of sparse recovery that correctly identifies systems in both small-noise and large-noise regimes.

**Keywords:** data-driven model selection, nonlinear dynamics, sparse recovery, generalized least squares, Galerkin method, adaptive grid, white noise

## 1. PROBLEM STATEMENT

Consider a first-order dynamical system in  $D$  dimensions of the form

$$\frac{d}{dt}\mathbf{x}(t) = \mathbf{F}(\mathbf{x}(t)), \quad \mathbf{x}(0) = \mathbf{x}_0 \in \mathbb{R}^D, \quad 0 \leq t \leq T, \quad (1.1)$$

and measurement data  $\mathbf{y} \in \mathbb{R}^{M \times D}$  given at  $M$  timepoints  $\mathbf{t} = [t_1, \dots, t_M]$  by

$$\mathbf{y}_{md} = \mathbf{x}_d(t_m) + \epsilon_{md}, \quad m \in [M], \quad d \in [D],$$

where throughout we use the bracket notation  $[M] := \{1, \dots, M\}$ . The matrix  $\epsilon \in \mathbb{R}^{M \times D}$  represents i.i.d. measurement noise. The focus of this article is the reconstruction of the dynamics (1.1) from the measurements  $\mathbf{y}$ .

The SINDy algorithm (Sparse Identification of Nonlinear Dynamics [4]) has been shown to be successful in solving this problem for sparsely represented nonlinear dynamics when noise is small and dynamic scales do not vary across multiple orders of magnitude. This framework assumes that the function  $\mathbf{F} : \mathbb{R}^D \rightarrow \mathbb{R}^D$  in (1.1) is given component-wise by

$$\mathbf{F}_d(\mathbf{x}(t)) = \sum_{j=1}^J \mathbf{w}^*_{jd} f_j(\mathbf{x}(t)) \quad (1.2)$$

for some known family of functions  $(f_j)_{j \in [J]}$  and a sparse weight matrix  $\mathbf{w}^* \in \mathbb{R}^{J \times D}$ . The problem is then transformed into solving for  $\mathbf{w}^*$  by building a data matrix  $\Theta(\mathbf{y}) \in \mathbb{R}^{M \times J}$  given by

$$\Theta(\mathbf{y})_{mj} = f_j(\mathbf{y}_m), \quad \mathbf{y}_m = (\mathbf{y}_{m1}, \dots, \mathbf{y}_{mD}),$$

so that the candidate functions are directly evaluated at the noisy data. Solving (1.1) for  $\mathbf{F}$  then reduces to solving

$$\dot{\mathbf{y}} = \Theta(\mathbf{y}) \widehat{\mathbf{w}} \quad (1.3)$$

for a sparse weight matrix  $\widehat{\mathbf{w}}$ , where  $\dot{\mathbf{y}}$  is the numerical time derivative of the data  $\mathbf{y}$ . Sequentially-thresholded least squares is then used to arrive at a sparse solution.

The automatic creation of an accurate mathematical model from data is a challenging task and research into statistically rigorous model selection can be traced back to Akaike's seminal work in the 1970's [1, 2]. In the last 20 years, there has been substantial work in this area at the interface between applied mathematics and statistics (see [3, 8, 9, 13, 15, 16] for both theory and applications). More recently, the formulation of system discovery problems in terms of a candidate basis of nonlinear functions (1.2) and subsequent discretization (1.3) was introduced in [14] in the context of catastrophe prediction. The authors of [14] used compressed sensing techniques to enforce sparsity. Since then there has been an explosion of interest in the problem of identifying nonlinear dynamical systems from data, with some of the primary techniques being Gaussian process regression [10], deep neural networks [11], Bayesian inference [18, 19] and a variety of methods from numerical analysis [6, 7]. These techniques have been successfully applied to discovery of both ordinary and partial differential equations. The variety of approaches qualitatively differ in the interpretability of the resulting data-driven dynamical system, the practicality of the algorithm, and the robustness due to noise, scale separation, etc. For instance, a neural-network based data-driven dynamical system does not easily lend itself to physical interpretation. As well, certain sparsification techniques are not practical to the general scientific community, where the problem of system identification from data is ubiquitous. The SINDy algorithm allows for direct interpretations of the dynamics from identified differential equations and uses sequentially thresholded least-squares to enforce sparsity, which is not nearly as robust as other approaches but is easy to implement and has been proven to converge to sparse local minimizers in [17]. Therefore, for simplicity we use sequential thresholding in this article to demonstrate the viability of our proposed weak formulation. Naturally one could investigate using a more robust sparsification strategy.

The aim of the present article is to provide rigorous justification for using the weak formulation of the dynamics in place of local pointwise derivative approximations, as well as a robust algorithm for doing so. As such, we restrict numerical experiments to autonomous ordinary differential equations for their immenability to analysis. Natural next steps are to explore identification of PDEs and non-autonomous dynamical systems. We note that the use of integral equations for system identification was introduced in [12], where compressed sensing techniques were used to enforce sparsity, and that this technique can be seen as a special case of the method introduced here. In Section 2 we introduce the algorithm with analysis of the resulting error structure and in Section 3 we provide numerical experimentation with a range of nonlinear systems. In Section 4, we provide concluding remarks including a brief comparison between WSINDy and conventional SINDy as well as natural next directions for this line of research.

## 2. WEAK SINDY

We approach the problem of system identification (1.3) from a non-standard perspective by utilizing the weak form of the differential equation. Recall that for any smooth test function  $\phi : \mathbb{R} \rightarrow \mathbb{R}$  (absolutely continuous is sufficient) and interval  $(a, b) \subset [0, T]$ , equation (1.1) admits the weak formulation

$$\phi(b)\mathbf{x}(b) - \phi(a)\mathbf{x}(a) - \int_a^b \phi'(u) \mathbf{x}(u) du = \int_a^b \phi(u) \mathbf{F}(\mathbf{x}(u)) du, \quad 0 \leq a < b \leq T. \quad (2.1)$$

With  $\phi = 1$ , we arrive at the integral equation of the dynamics explored in [12]. If we instead take  $\phi$  to be non-constant and compactly supported in  $(a, b)$ , we arrive at

$$- \int_a^b \phi'(u) \mathbf{x}(u) du = \int_a^b \phi(u) \mathbf{F}(\mathbf{x}(u)) du. \quad (2.2)$$

We then define the generalized residual  $\mathcal{R}(\mathbf{w}; \phi)$  for a given test function by replacing  $\mathbf{F}$  with a candidate element from the span of  $(f_j)_{j \in [J]}$  and  $\mathbf{x}$  with  $\mathbf{y}$  as follows:

$$\mathcal{R}(\mathbf{w}; \phi) := \int_a^b \left( \phi'(u) \mathbf{y}(u) + \phi(u) \left( \sum_{j=1}^J \mathbf{w}_j f_j(\mathbf{y}(u)) \right) \right) du. \quad (2.3)$$

Clearly with  $\mathbf{w} = \mathbf{w}^*$  and  $\mathbf{y} = \mathbf{x}(t)$  we have  $\mathcal{R}(\mathbf{w}; \phi) = 0$  for all  $\phi$  compactly-supported in  $(a, b)$ ; however,  $\mathbf{y}$  is a discrete set of data, hence (2.3) can at best be approximated numerically, with measurement noise presenting a significant barrier to accurate identification of  $\mathbf{w}^*$ .

**2.1. Method Overview.** For analogy with traditional Galerkin methods, consider the forward problem of solving a dynamical system such as (1.1) for  $\mathbf{x}$ . The Galerkin approach is to seek a solution  $\mathbf{x}$  represented in a chosen trial basis  $(f_j)_{j \in [J]}$  such that the residual  $\mathcal{R}$ , defined by

$$\mathcal{R} = \int \phi(t)(\dot{\mathbf{x}}(t) - \mathbf{F}(\mathbf{x}(t))) dt,$$

is minimized over all test functions  $\phi$  living in the span of a given test function basis  $(\phi_k)_{k \in [K]}$ . If the trial and test function bases are known analytically, inner products of the form  $\langle f_j, \phi_k \rangle$  appearing in the residual can be computed exactly. Thus, the computational error results only from representing the solution in a finite-dimensional function space.

The method we present here can be considered a data-driven Galerkin method of solving for  $\mathbf{F}$  where the trial ‘‘basis’’ is given by the set of gridfunctions  $(f_j(\mathbf{y}))_{j \in [J]}$  evaluated at the data and only the test-function basis  $(\phi_k)_{k \in [K]}$  is known analytically. In this way, inner products appearing in  $\mathcal{R}(\mathbf{w}; \phi)$  must be approximated numerically, implying that the accuracy of the recovered weights  $\hat{\mathbf{w}}$  is ultimately limited by the quadrature scheme used to discretize inner products. Using Lemma 2 below, we show that the correct coefficients  $\mathbf{w}^*$  may be recovered to effective machine precision accuracy (given by the tolerance of the forward ODE solver) from noise-free trajectories  $\mathbf{y}$  by discretizing (2.2) using the trapezoidal rule and choosing  $\phi$  to decay smoothly to zero at the boundaries of its support. In this article we demonstrate this fact by choosing test functions from a particular family of unimodal piece-wise polynomials  $\mathcal{S}$  defined in (2.6).

Having chosen a quadrature scheme, the next accuracy barrier is presented by measurement noise, which introduces a bias in the weights. Below we analyze the distribution of the residuals  $\mathcal{R}(\mathbf{w}; \phi)$  to arrive at a generalized least squares approach where an approximate covariance matrix can be computed directly from the test functions. This analysis also shows that placing test functions near steep gradients in the dynamics improves recovery, hence we develop a self-consistent and stable algorithm for constructing a test function basis adaptively near these regions which also does not rely on pointwise approximation of derivatives. Overall, we show that when noise is present, our method produces a recovered weight matrix  $\hat{\mathbf{w}}$  with the number of significant digits scaling optimally with the signal-to-noise ratio  $\sigma_{SNR}$  (defined below).

*Remark 1.* The weak formulation of the dynamics introduces a wealth of information: given  $M$  timepoints  $\mathbf{t} = (t_m)_{m \in [M]}$ , equation (2.2) affords  $K = M(M - 1)/2$  residuals over all possible supports  $(a, b) \subset \mathbf{t} \times \mathbf{t}$  with  $a < b$ . Of course, one could also assimilate the responses of multiple families of test functions  $(\{\phi_k^1\}_{k \in [K_1]}, \{\phi_k^2\}_{k \in [K_2]}, \dots)$ ; however, the computational complexity of such an exhaustive approach quickly becomes intractable. We stress that even with large noise, our proposed method identifies the correct nonlinearities with accurate weight recovery while keeping the number of test functions much lower than the number of timepoints ( $K \ll M$ ).

**2.2. Algorithm: Weak SINDy.** We state here the Weak SINDy algorithm in full generality. We propose a generalized least squares approach with approximate covariance matrix  $\Sigma$ . Below we derive a particular choice of  $\Sigma$  which utilizes the action of the test functions  $(\phi_k)_{k \in [K]}$  on the data  $\mathbf{y}$ . Sequential thresholding on the weight coefficients  $\mathbf{w}$  with thresholding parameter  $\lambda$  is used to enforce sparsity. In addition, an  $\ell_2$ -regularization term with coefficient  $\gamma$  is included for problems involving rank deficiency. Methods of choosing optimal  $\lambda$  and  $\gamma$  are not included in this study. We note that  $\lambda < \min_{\mathbf{w}^* \neq 0} |\mathbf{w}^*|$  is necessary for recovery and that with low noise our method is not sensitive to  $\lambda$ . Throughout we mostly set  $\gamma = 0$ , however some problems do require regularization, such as the Lotka-Volterra system.

$\hat{\mathbf{w}} = \mathbf{WSINDy}(\mathbf{y}, \mathbf{t}; (\phi_k)_{k \in [K]}, (f_j)_{j \in [J]}, \Sigma, \lambda, \gamma)$ :

- (1) Construct matrix of trial gridfunctions  $\Theta(\mathbf{y}) = [f_1(\mathbf{t}, \mathbf{y}) \mid \dots \mid f_J(\mathbf{t}, \mathbf{y})]$
- (2) Construct integration matrices  $\mathbf{V}, \mathbf{V}'$  such that

$$\mathbf{V}_{km} = \Delta t \phi_k(t_m), \quad \mathbf{V}'_{km} = \Delta t \phi'_k(t_m)$$

- (3) Compute Gram matrix  $\mathbf{G} = \mathbf{V}\Theta(\mathbf{y})$  and right-hand side  $\mathbf{b} = -\mathbf{V}'\mathbf{y}$  so that  $\mathbf{G}_{kj} = \langle \phi_k, f_j(\mathbf{y}) \rangle$  and  $\mathbf{b}_{kd} = -\langle \phi'_k, \mathbf{y}_d \rangle$
- (4) Solve the generalized least-squares problem with  $\ell_2$ -regularization

$$\hat{\mathbf{w}} = \operatorname{argmin}_{\mathbf{w}} \left\{ (\mathbf{G}\mathbf{w} - \mathbf{b})^T \Sigma^{-1} (\mathbf{G}\mathbf{w} - \mathbf{b}) + \gamma^2 \|\mathbf{w}\|_2^2 \right\},$$

using sequential thresholding with parameter  $\lambda$  to enforce sparsity.

With this as our core algorithm, we can now consider a residual analysis (Section 2.3) leading to a weighted least squares solution. We can also develop theoretical results related to the test functions (Section 2.4),

yielding a more thorough understanding of the impact of using uniform (Section 2.4.1) and adaptive (Section 2.4.2) placement of test functions along the time axis.

**2.3. Residual Analysis.** Performance of WSINDy is determined by the behavior of the residuals

$$\mathcal{R}(\mathbf{w}; \phi_k) := (\mathbf{G}\mathbf{w} - \mathbf{b})_k \in \mathbb{R}^{1 \times D},$$

denoted  $\mathcal{R}(\mathbf{w}) \in \mathbb{R}^{K \times D}$  for the entire residual matrix. Here we analyze the residual to highlight key aspects for future analysis, as well as to arrive at an appropriate choice of approximate covariance  $\Sigma$ . We also provide a heuristic argument in favor of placing test functions near steep gradients in the dynamics.

A key difficulty in recovering the true weights  $\mathbf{w}^*$  is that in general,  $\mathbb{E}[\mathcal{R}(\mathbf{w}^*)] \neq 0$  due to nonlinearities present in  $\Theta(\mathbf{y})$ , thus the recovered weights  $\hat{\mathbf{w}}$  will be inherently biased. Nevertheless, we can isolate the dominant error terms by expanding out the residual and linearizing around the true trajectory  $\mathbf{x}(t)$ :

$$\begin{aligned} \mathcal{R}(\mathbf{w}; \phi_k) &= \langle \phi_k, \Theta(\mathbf{y})\mathbf{w} \rangle + \langle \phi'_k, \mathbf{y} \rangle \\ &= \langle \phi_k, \Theta(\mathbf{y})(\mathbf{w} - \mathbf{w}^*) \rangle + \langle \phi_k, \Theta(\mathbf{y})\mathbf{w}^* \rangle + \langle \phi'_k, \mathbf{y} \rangle \\ &= \underbrace{\langle \phi_k, \Theta(\mathbf{y})(\mathbf{w} - \mathbf{w}^*) \rangle}_{R_1} + \underbrace{\langle \phi_k, \epsilon \nabla \mathbf{F}(\mathbf{x}) \rangle}_{R_2} + \underbrace{\langle \phi'_k, \epsilon \rangle}_{R_3} + I_k + \mathcal{O}(\epsilon^2) \end{aligned}$$

where  $\nabla F(\mathbf{x})_{d'd} = \frac{\partial \mathbf{F}_d}{\partial \mathbf{x}_{d'}}(\mathbf{x})$ . The errors manifest in the following ways:

- $R_1$  is the misfit between  $\mathbf{w}$  and  $\mathbf{w}^*$
- $R_2$  results from measurement error in trial gridfunctions  $f_j(\mathbf{y}) = f_j(\mathbf{x} + \epsilon)$
- $R_3$  results from replacing  $\mathbf{x}$  with  $\mathbf{y} = \mathbf{x} + \epsilon$  in the left-hand side of (2.2)
- $I_k$  is the integration error
- $\mathcal{O}(\epsilon^2)$  is the remainder term in the truncated Taylor expansion of  $\mathbf{F}(\mathbf{y})$  around  $\mathbf{x}$ :

$$\mathbf{F}(\mathbf{y}_m) = \mathbf{F}(\mathbf{x}(t_m)) + \epsilon_m \nabla \mathbf{F}(\mathbf{x}(t_m)) + \mathcal{O}(|\epsilon_m|^2).$$

Clearly, recovery of  $\mathbf{F}$  when  $\epsilon = 0$  is straight forward:  $R_1$  and  $I_k$  are the only error terms, thus one only needs to select a quadrature scheme that ensures that the integration error  $I_k$  is negligible and  $\hat{\mathbf{w}} = \mathbf{w}^*$  will be the minimizer. A primary focus of this study is the use of a specific family of piecewise polynomial test functions  $\mathcal{S}$  defined below for which the trapezoidal rule is highly accurate (see Lemma 2). Figure 3.1 demonstrates this fact on noise-free data.

For  $\epsilon > 0$ , accurate recovery of  $\mathbf{F}$  requires one to choose hyperparameters that exemplify the true misfit term  $R_1$  by enforcing that the other error terms are of lower order. We look for  $(\phi_k)_{k \in [K]}$  and  $\Sigma = \mathbf{C}\mathbf{C}^T$  that approximately enforce  $\mathbf{C}^{-1}\mathcal{R}(\mathbf{w}^*) \sim \mathcal{N}(0, \sigma^2\mathbf{I})$ , justifying the least squares approach. In the next subsection we address the issue of approximating the covariance matrix, providing justification for using  $\Sigma = \mathbf{V}'(\mathbf{V}')^T$ . The following subsection provides a heuristic argument for how to reduce corruption from the error terms  $R_2$  and  $R_3$  by placing test functions near steep gradients in the data.

2.3.1. **Approximate Covariance**  $\Sigma$ . Neglecting  $I_k$  and  $\mathcal{O}(\epsilon^2)$ , we can rewrite  $\mathcal{R}(\mathbf{w}; \phi_k)$  with  $R_2$  and  $R_3$  together as

$$\mathcal{R}(\mathbf{w}; \phi_k) = R_1 + \mathbf{Z}_k = R_1 + \sum_{m=1}^M \epsilon_m \mathbf{T}_m \Delta t$$

where

$$\mathbf{T}_m = \phi'_k(t_m) \mathbf{I}_D + \phi_k(t_m) \nabla \mathbf{F}(\mathbf{x}(t_m))$$

is the linearized operator left-multiplying the noise vector

$$\epsilon_m = (\epsilon_{1m} \ \epsilon_{2m} \ \dots \ \epsilon_{Dm})$$

at timestep  $t_m$  and  $\mathbf{I}_D$  is the identity in  $\mathbb{R}^{D \times D}$ . The true distribution of  $\mathbf{Z}$  therefore depends on  $\nabla \mathbf{F}$ , which is not known *a priori*. For a leading order approximation we propose using  $\mathbf{T}_m \approx \phi'_k(t_m) \mathbf{I}_D$  which holds if  $\|\phi'_k\|_\infty \gg \|\phi_k\|_\infty$ . We then get that the columns of  $\mathbf{Z}$  (corresponding to errors in each component  $\mathbf{F}_d$  along the time series) are approximately i.i.d normal with mean zero and covariance  $\mathbf{V}'(\mathbf{V}')^T$ . For this reason, we adopt the heuristic  $\Sigma = \mathbf{V}'(\mathbf{V}')^T$ , or  $\Sigma_{ij} = \Delta t^2 \sum_{m=1}^M \phi'_i(t_m) \phi'_j(t_m) = \Delta t \langle \phi'_i, \phi'_j \rangle$ .

2.3.2. **Adaptive Refinement**. Next we show that by localizing  $\phi_k$  around large  $|\dot{\mathbf{x}}|$ , we get an approximate cancellation of the error terms  $R_2$  and  $R_3$ . Consider the one-dimensional case ( $D = 1$ ) where  $m$  is an arbitrary time index and  $\mathbf{y}_m = \mathbf{x}(t_m) + \epsilon$  is an observation. When  $|\dot{\mathbf{x}}(t_m)|$  is large compared to  $\epsilon$ , we approximately have

$$\mathbf{y}_m = \mathbf{x}(t_m) + \epsilon_m \approx \mathbf{x}(t_m + \delta t) \approx \mathbf{x}(t_m) + \delta t \mathbf{F}(\mathbf{x}(t_m)) \quad (2.4)$$

for some small  $\delta t$ , i.e. the perturbed value  $\mathbf{y}_m$  lands close to the true trajectory  $\mathbf{x}$  at the time  $t_m + \delta t$ . To understand the heuristic behind this approximation, let  $\delta t$  be the point of intersection between the tangent line to  $\mathbf{x}(t)$  at  $t_m$  and  $\mathbf{x}(t_m) + \epsilon$ . Then

$$\delta t = \frac{\epsilon}{\dot{\mathbf{x}}(t_m)},$$

hence  $|\dot{\mathbf{x}}(t_m)| \gg \epsilon$  implies that  $\mathbf{x}(t_m) + \epsilon$  will approximately lie on the true trajectory. As well, regions where  $|\dot{\mathbf{x}}(t_m)|$  is small will not yield accurate recovery in the case of noisy data, since perturbations are more likely to exit the relevant region of phase space. If we linearize  $\mathbf{F}$  using the approximation (2.4) we get

$$\mathbf{F}(\mathbf{y}_m) \approx \mathbf{F}(\mathbf{x}(t_m)) + \delta t \mathbf{F}'(\mathbf{x}(t_m)) \mathbf{F}(\mathbf{x}(t_m)) = \mathbf{F}(\mathbf{x}(t_m)) + \delta t \ddot{\mathbf{x}}(t_m). \quad (2.5)$$

Assuming  $\phi_k$  is sufficiently localized around  $t_m$ , (2.4) also implies that

$$\langle \phi'_k, \mathbf{x} \rangle + \underbrace{\langle \phi'_k, \epsilon \rangle}_{R_3} = \langle \phi'_k, \mathbf{y} \rangle \approx \langle \phi'_k, \mathbf{x} \rangle + \delta t \langle \phi'_k, \mathbf{F}(\mathbf{x}) \rangle,$$

hence  $R_3 \approx \delta t \langle \phi'_k, \mathbf{F}(\mathbf{x}) \rangle$ , while (2.5) implies

$$\begin{aligned} \langle \phi_k, \Theta(\mathbf{y}) \mathbf{w} \rangle &= \underbrace{\langle \phi_k, \Theta(\mathbf{y})(\mathbf{w} - \mathbf{w}^*) \rangle}_{=R_2} + \langle \phi_k, \mathbf{F}(\mathbf{y}) \rangle \\ &\approx \langle \phi_k, \Theta(\mathbf{y})(\mathbf{w} - \mathbf{w}^*) \rangle + \langle \phi_k, \mathbf{F}(\mathbf{x}) \rangle + \underbrace{\delta t \langle \phi_k, \ddot{\mathbf{x}} \rangle}_{\approx R_2} \\ &= \langle \phi_k, \Theta(\mathbf{y})(\mathbf{w} - \mathbf{w}^*) \rangle + \langle \phi_k, \mathbf{F}(\mathbf{x}) \rangle - \delta t \langle \phi'_k, \mathbf{F}(\mathbf{x}) \rangle \end{aligned}$$

having integrated by parts. Collecting the terms together yields that the residual takes the form

$$\mathcal{R}(\mathbf{w}; \phi_k) = \langle \phi'_k, \mathbf{y} \rangle + \langle \phi_k, \Theta(\mathbf{y})\mathbf{w} \rangle \approx R_2,$$

and we see that  $R_2$  and  $R_3$  have effectively canceled. In higher dimensions this interpretation does not appear to be as illuminating, but nevertheless, for any given coordinate  $\mathbf{x}_d$ , it does hold that terms in the error expansion vanish around points  $t_m$  where  $|\dot{\mathbf{x}}_d|$  is large, precisely because  $\mathbf{x}_d(t_m) + \epsilon \approx \mathbf{x}_d(t_m + \delta t)$ .

**2.4. Test Function Basis**  $(\phi_k)_{k \in [K]}$ . Here we introduce a test function space  $\mathcal{S}$  and quadrature scheme to minimize integration errors and enact the heuristic arguments above, which rely on  $\phi_k$  sufficiently localized and satisfying  $|\phi'_k| \gg |\phi_k|$ . We define the space  $\mathcal{S}$  of unimodal piece-wise polynomials of the form

$$\phi(t) = \begin{cases} C(t-a)^p(b-t)^q & t \in (a, b), \\ 0 & \text{otherwise,} \end{cases} \quad (2.6)$$

where  $(a, b) \subset \mathbf{t} \times \mathbf{t}$  satisfies  $a < b$  and  $p, q \geq 1$ . The normalization

$$C = \frac{1}{p^p q^q} \left( \frac{p+q}{b-a} \right)^{p+q}$$

ensures that  $\|\phi\|_\infty = 1$ . Functions  $\phi \in \mathcal{S}$  are non-negative, unimodal, and compactly supported in  $[0, T]$  with  $\lfloor \min\{p, q\} \rfloor - 1$  continuous derivatives. Larger  $p$  and  $q$  imply faster decay towards the endpoints of the support.

To ensure the integration error in approximating inner products  $\langle f_j, \phi_k \rangle$  is negligible, we rely on the following lemma, which provides a bound on the error in discretizing the weak derivative relation

$$- \int \phi' f dt = \int \phi f' dt \quad (2.7)$$

using the trapezoidal rule for compactly supported  $\phi$ . Following the lemma we introduce two strategies for choosing the parameters of the test functions  $(\phi_k)_{k \in [K]} \subset \mathcal{S}$ .

**Lemma 2** (Numerical Error in Weak Derivatives). *Let  $f, \phi$  have continuous derivatives of order  $p$  and define  $t_j = a + j \frac{b-a}{N} = a + j \Delta t$ . Then if  $\phi$  has roots  $\phi(a) = \phi(b) = 0$  of multiplicity  $p$ , then*

$$\frac{\Delta t}{2} \sum_{j=0}^{N-1} [g(t_j) + g(t_{j+1})] = \mathcal{O}(\Delta t^{p+1}), \quad (2.8)$$

where  $g(t) = \phi'(t)f(t) + \phi(t)f'(t)$ . In other words, the composite trapezoidal rule discretizes the weak derivative relation (2.7) to order  $p+1$ .

*Proof.* This is a simple consequence of the Euler-Maclaurin formula. If  $g : [a, b] \rightarrow \mathbb{C}$  is a smooth function, then

$$\frac{\Delta t}{2} \sum_{j=0}^{N-1} [g(t_j) + g(t_{j+1})] \sim \int_a^b g(t) dt + \sum_{k=1}^{\infty} \frac{\Delta t^{2k} B_{2k}}{(2k)!} \left( g^{(2k-1)}(b) - g^{(2k-1)}(a) \right),$$

where  $B_{2k}$  are the Bernoulli numbers. The asymptotic expansion provides corrections to the trapezoidal rule that realize machine precision accuracy up until a certain value of  $k$ , after which terms in the expansion

grow and the series diverges [5, Ch. 3]. In our case,  $g(t) = \phi'(t)f(t) + \phi(t)f'(t)$  where the root conditions on  $\phi$  imply that

$$\int_a^b g(t) dt = 0 \quad \text{and} \quad g^{(k)}(b) = g^{(k)}(a) = 0, \quad 0 \leq k \leq p-1.$$

So for  $p$  odd, we have that

$$\begin{aligned} \frac{\Delta t}{2} \sum_{j=0}^{N-1} [g(t_j) + g(t_{j+1})] &\sim \sum_{k=(p+1)/2}^{\infty} \frac{\Delta t^{2k} B_{2k}}{(2k)!} \left( g^{(2k-1)}(b) - g^{(2k-1)}(a) \right) \\ &= \frac{B_{p+1}}{(p+1)!} (\phi^{(p)}(b)f(b) - \phi^{(p)}(a)f(a)) \Delta t^{p+1} + \mathcal{O}(\Delta t^{p+2}). \end{aligned}$$

For even  $p$ , the leading term is  $\mathcal{O}(\Delta t^{p+2})$  with a slightly different coefficient. □

For  $\phi \in \mathcal{S}$  with  $p = q$ , the exact leading order error in term in (2.8) is

$$\frac{2^p B_{p+1}}{p+1} (f(b) - f(a)) \Delta t^{p+1},$$

which is negligible for a wide range of reasonable  $p$  and  $\Delta t$  values. The Bernoulli numbers eventually start growing like  $p^p$ , but for smaller values of  $p$  they are moderate. For instance, with  $\Delta t = 0.1$  and  $f(b) - f(a) = 1$ , this error term is  $o(1)$  up until  $p = 85$ , where it takes the value 0.495352, while for  $\Delta t = 0.01$ , the error is below machine precision for all  $p$  between 7 and 819. For these reasons, in what follows we choose test functions  $(\phi_k)_{k \in [K]} \subset \mathcal{S}$  and discretize all integrals using the trapezoidal rule. Unless otherwise stated, each function  $\phi_k$  satisfies  $p = q$  and so is fully determined by the tuple  $\{p_k, a_k, b_k\}$  indicating its polynomial degree and support. In the next two subsections we propose two different strategies for determining  $\phi_k$  using the data  $\mathbf{y}$ .

**2.4.1. Strategy 1: Uniform Grid.** The simplest strategy for choosing a test function basis  $(\phi_k)_{k \in [K]} \subset \mathcal{S}$  is to place  $\phi_k$  uniformly on the interval  $[0, T]$  with fixed degree  $p$  and support size  $L$  denoting the number of timepoints in  $\mathbf{t}$  that each  $\phi_k$  is supported on. Specifically we propose the following three steps to automate this process, requiring only that the user specify the polynomial degree  $p$  and the total number of basis functions  $K$ , through the values of two hyperparameters  $\rho$  and  $s$  that relate to the residual analysis above.

*Step 1: Choosing  $L$ :* We propose to fix the support size of each  $\phi_k$  to be

$$L = \frac{1}{2} \left( \frac{M}{\operatorname{argmax}_n |\mathbf{Y}|_n} \right) \tag{2.9}$$

where  $|\mathbf{Y}|_n$  is the magnitude of the  $n$ th Fourier mode of  $\mathbf{y}$  minus its mean. In this way the action of the test functions exploits that large changes in the dynamics are most likely to occur within time intervals of length equal to the largest Fourier mode.

*Step 2: Determining  $p$ :* In light of the derivation above of the approximate covariance matrix  $\Sigma$ , we define  $\rho := \|\phi'_k\|_{\infty} / \|\phi_k\|_{\infty}$ , where larger  $\rho$  indicates better agreement with  $\Sigma$ . The value of  $\rho$  selects the polynomial degree  $p$  as follows: analytically,

$$\rho = \frac{2\sqrt{2p-1}}{b-a} \left( \frac{1-1/p}{1-1/2p} \right)^{p-1} = \frac{1.67 \dots}{b-a} \left( p^{1/2} + p^{-1/2} \right) + o(p^{-1/2}).$$

As a leading order approximate we set  $p = \lceil \rho^2 \frac{|b-a|^2}{2.8} \rceil$ .



*Step 3: Determining  $K$ :* Next we introduce the shift parameter  $s \in [0, 1]$  defined by

$$s = \phi_k(t^*) = \phi_{k+1}(t^*),$$

which determines  $K$  from  $p$  and  $L$ . In words,  $s$  is the height of intersection between  $\phi_k$  and  $\phi_{k+1}$  and measures the amount of overlap between successive test functions, which factors into the covariance matrix  $\Sigma$ . This fixes  $a_{k+1} - a_k = \Delta t L \sqrt{1 - s^{1/p}}$  for each pair of neighboring test functions. Larger  $s$  implies that neighboring basis functions overlap on more points, with  $s = 1$  indicating that  $\phi_k = \phi_{k+1}$ . Specifically, neighboring basis functions overlap on  $\lfloor L(1 - \sqrt{1 - s^{1/p}}) \rfloor$  timepoints.

In Figures 3.2 and 3.3 we vary the parameters  $\rho$  and  $s$  and observe that results agree with intuition: larger  $\rho$  and larger  $s$  lead to better recovery of  $\mathbf{w}^*$ .

$\hat{\mathbf{w}} = \mathbf{WSINDy\_UG}(\mathbf{y}, \mathbf{t}; (f_j)_{j \in [J]}, \rho, s, \lambda, \gamma)$ :

- (1) Construct matrix of trial gridfunctions  $\Theta(\mathbf{y}) = [f_1(\mathbf{t}, \mathbf{y}) \mid \dots \mid f_J(\mathbf{t}, \mathbf{y})]$
- (2) Construct integration matrices  $\mathbf{V}, \mathbf{V}'$  such that

$$\mathbf{V}_{km} = \Delta t \phi_k(t_m), \quad \mathbf{V}'_{km} = \Delta t \phi'_k(t_m)$$

with the test functions  $(\phi_k)_{k \in [K]}$  determined by  $\rho, s$  as described above

- (3) Compute Gram matrix  $\mathbf{G} = \mathbf{V}\Theta(\mathbf{y})$  and right-hand side  $\mathbf{b} = -\mathbf{V}'\mathbf{y}$  so that  $\mathbf{G}_{kj} = \langle \phi_k, f_j(\mathbf{y}) \rangle$  and  $\mathbf{b}_{kd} = -\langle \phi'_k, \mathbf{y}_d \rangle$
- (4) Compute approximate covariance and Cholesky factorization  $\Sigma = \mathbf{V}'(\mathbf{V}')^T = \mathbf{C}\mathbf{C}^T$
- (5) Solve the generalized least-squares problem with  $\ell_2$ -regularization

$$\hat{\mathbf{w}} = \operatorname{argmin}_{\mathbf{w}} \left\{ (\mathbf{G}\mathbf{w} - \mathbf{b})^T \Sigma^{-1} (\mathbf{G}\mathbf{w} - \mathbf{b}) + \gamma^2 \|\mathbf{w}\|_2^2 \right\},$$

using sequential thresholding with parameter  $\lambda$  to enforce sparsity.

**2.4.2. Strategy 2: Adaptive Grid.** Motivated by the arguments above, we now introduce an algorithm for constructing a test function basis localized near points of large change in the dynamics. This occurs in three steps: 1) construct a weak approximation to the derivative of the dynamics  $\mathbf{v} \approx \dot{\mathbf{x}}$ , 2) sample  $K$  points  $\mathbf{c}$  from a cumulative distribution  $\psi$  with density proportional to the total variation  $|\mathbf{v}|$ , 3) construct test functions centered at  $\mathbf{c}$  using a width-at-half-max parameter  $r_{whm}$  to determine the parameters  $(p_k, a_k, b_k)$  of each basis function  $\phi_k$ . Each of these steps is numerically stable and carried out independently along each coordinate of the dynamics. A visual diagram is provided in Figure 2.1.

*Step 1: Weak Derivative Approximation:* Define  $\mathbf{v} := -\mathbf{V}'_p \mathbf{y}$ , where the matrix  $-\mathbf{V}'_p$  enacts a linear convolution with the derivative of a piece-wise polynomial test function  $\phi \in \mathcal{S}$  of degree  $p$  and support size  $s$  so that

$$\mathbf{v}_m = -\langle \phi', \mathbf{y} \rangle = \langle \phi, \dot{\mathbf{y}} \rangle \approx \dot{\mathbf{y}}_m.$$

The parameters  $s$  and  $p$  are chosen by the user, with  $s = 4$  and  $p \geq 2$  corresponding to taking a centered finite difference derivative with 3-point stencil. Larger  $s$  results in more smoothing and minimizes the corruption from noise while still capturing the correct large deviations in the dynamics. For all examples we let  $p = 2$  and  $s = 16$  and note that greater disparity between  $p$  and  $s$  results in more pronounced localization (less

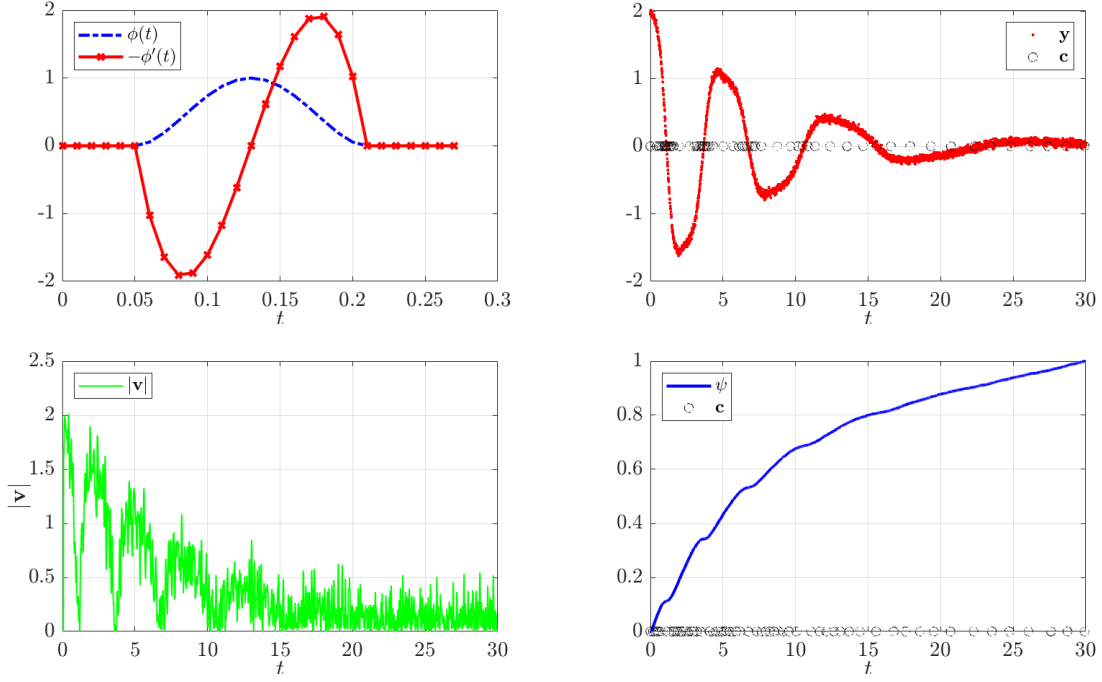


FIGURE 2.1. Counter-clockwise from top left: test function  $\phi$  and derivative  $-\phi'$  used to compute  $\mathbf{v}$ , approximate total variation  $|\mathbf{v}|$ , cumulative distribution  $\psi = \int^t |\mathbf{v}| dt$ , noisy data  $\mathbf{y}$  from the Duffing equation and resulting test functions centers  $\mathbf{c}$ . As desired, the centers  $\mathbf{c}$  are clustered near steep gradients in the dynamics despite measurement noise.

uniform distribution) of test functions.

*Step 2: Selecting  $\mathbf{c}$ :* Having computed  $\mathbf{v}$ , define  $\psi$  to be the cumulative sum of  $|\mathbf{v}|$  normalized so that  $\max \psi = 1$ . In this way  $\psi$  is a valid cumulative distribution function with density proportional to the total variation of  $\mathbf{y}$ . We then find  $\mathbf{c}$  by sampling from  $\psi$ . Let  $U = [0, \frac{1}{K}, \frac{2}{K}, \dots, \frac{K-1}{K}]$  with  $K$  being the number of the test functions, we then define  $\mathbf{c} = \psi^{-1}(U)$ , or numerically,

$$c_k = \min\{t \in \mathbf{t} : \psi(t) \geq U_k\}.$$

This stage requires the user to select the number of test functions  $K$ .

*Step 3: Construction of Test functions  $(\phi_k)_{k \in [K]}$ :* Having chosen the location  $c_k$  of the centerpoint for each test function  $\phi_k$ , we are left to choose the degree  $p_k$  of the polynomial and the supports  $[a_k, b_k]$ . The degree is chosen according to the width-at-half-max parameter  $r_{whm}$ , which specifies the difference in timepoints between each center  $c_k$  and  $\arg_t\{\phi_k(t) = 1/2\}$ , while the supports are chosen such that  $\phi_k(b_k - \Delta t) = 10^{-16}$ . This gives us a nonlinear system of two equations in two unknowns which can be easily solved (i.e. using MATLAB's `fzero`). This can be done for one reference test functions and the rest of the weights obtained by translation.

The adaptive grid Weak SINDy algorithm is summarized as follows:

$\widehat{\mathbf{w}} = \mathbf{WSINDy\_AG}(\mathbf{y}, \mathbf{t}; (f_j)_{j \in [J]}, p, s, K, r_{whm}, \lambda, \gamma)$ :

- (1) Construct matrix of trial gridfunctions  $\Theta(\mathbf{y}) = [f_1(\mathbf{t}, \mathbf{y}) \mid \dots \mid f_J(\mathbf{t}, \mathbf{y})]$
- (2) Construct integration matrices  $\mathbf{V}, \mathbf{V}'$  such that

$$\mathbf{V}_{km} = \Delta t \phi_k(t_m), \quad \mathbf{V}'_{km} = \Delta t \phi'_k(t_m),$$

with test functions  $(\phi_k)_{k \in [K]}$  determined by  $p, s, K, r_{whm}$  as described above

- (3) Compute Gram matrix  $\mathbf{G} = \mathbf{V}\Theta(\mathbf{y})$  and right-hand side  $\mathbf{b} = -\mathbf{V}'\mathbf{y}$  so that  $\mathbf{G}_{kj} = \langle \phi_k, f_j(\mathbf{y}) \rangle$  and  $\mathbf{b}_{kd} = -\langle \phi'_k, \mathbf{y}_d \rangle$
- (4) Compute approximate covariance and Cholesky factorization  $\Sigma = \mathbf{V}'(\mathbf{V}')^T = \mathbf{C}\mathbf{C}^T$
- (5) Solve the generalized least-squares problem with  $\ell_2$ -regularization

$$\widehat{\mathbf{w}} = \operatorname{argmin}_{\mathbf{w}} \left\{ (\mathbf{G}\mathbf{w} - \mathbf{b})^T \Sigma^{-1} (\mathbf{G}\mathbf{w} - \mathbf{b}) + \gamma^2 \|\mathbf{w}\|_2^2 \right\},$$

using sequential thresholding with parameter  $\lambda$  to enforce sparsity.

The parameters  $p$  and  $s$  play a role in determining how localized the test function basis is around steep gradients and ultimately depend on the timestep  $\Delta t$ . As mentioned above, we set  $p = 2$  and  $s = 16$  throughout as this produces sufficient localization for the examples featured in this article. For simplicity we fix the number of test functions  $K$  to be a multiple of the number of trial functions (i.e.  $K = J, 2J, 3J$  etc.). For larger noise it is necessary to use a larger basis, while for small noise it is often sufficient to set  $K = J$ . The optimal value of  $r_{whm}$  depends on the timescales of the dynamics and can be chosen from the data using the Fourier transform as in the uniform grid case, however for simplicity we set  $r_{whm} = 30$  throughout.

### 3. NUMERICAL EXPERIMENTS

We now show that WSINDy is capable of recovering the correct dynamics to high accuracy over a range of signal-to-noise ratios. To generate true trajectory data we use MATLAB's `ode45` with absolute and relative tolerance  $1e-10$  and sampling rate of  $\Delta t = 0.01$ , unless otherwise specified. We choose a fixed sampling rate  $\Delta t$  for simplicity and uniformity across examples but note that a detailed study of the dependency of the algorithm on  $\Delta t$  is not presented here. While the results in this section hold for a wide range of  $\Delta t$  (results not presented here), different sampling rates may result in different choices of hyperparameters (e.g.,  $\rho$  and  $s$  in the case of WSINDy\_UG). White Gaussian noise with mean zero and variance  $\sigma^2$  is then added to the exact trajectories, where  $\sigma$  is computed by specifying the signal-to-noise ratio  $\sigma_{SNR}$  and setting

$$\sigma = \sigma_{SNR} \|\mathbf{x}\|_{RMS} \quad \text{where} \quad \|\mathbf{x}\|_{RMS} = \sqrt{\frac{1}{DM} \sum_{d=1}^D \sum_{m=1}^M |\mathbf{x}_d(t_m)|^2}.$$

In this way,  $\|\epsilon\|_{RMS} / \|\mathbf{x}\|_{RMS} \approx \sigma$ . We examine the following canonical nonlinear systems with variations in the specified parameters:

$$\begin{array}{l}
\text{Duffing} \\
\text{Van der Pol} \\
\text{Lotka-Volterra} \\
\text{Lorenz}
\end{array}
\begin{cases}
\dot{x}_1 = x_2, \\
\dot{x}_2 = -\mu x_2 - \alpha x_1 - \beta x_1^3, \\
\dot{x}_1 = x_2, \\
\dot{x}_2 = \beta x_2(1 - x_1^2) - x_1, \\
\dot{x}_1 = \alpha x_1 - \beta x_1 x_2, \\
\dot{x}_2 = \beta x_1 x_2 - 2\alpha x_2, \\
\dot{x}_1 = \sigma(x_2 - x_1), \\
\dot{x}_2 = x_1(\rho - x_3) - x_2, \\
\dot{x}_3 = x_1 x_2 - \beta x_3,
\end{cases}
\begin{array}{l}
\text{variable } \beta, \\
\text{variable } \beta, \\
\text{variable } \beta, \\
\text{variable } \mathbf{x}(0),
\end{array}
\begin{array}{l}
\text{fixed } \mu = 0.2, \alpha = 0.05, \mathbf{x}(0) = \begin{bmatrix} 0 \\ 2 \end{bmatrix} \\
\text{fixed } \mathbf{x}(0) = \begin{bmatrix} 0 \\ 1 \end{bmatrix} \\
\text{fixed } \alpha = 1, \mathbf{x}(0) = \begin{bmatrix} 1 \\ 2 \end{bmatrix} \\
\text{fixed } \sigma = 10, \beta = 8/3, \rho = 28
\end{array}$$

The Duffing equation and Van der Pol oscillator present cases of approximately linear systems with cubic nonlinearities. Solutions to the Van der Pol oscillator and Lotka-Volterra system exhibit orbits with variable speed of motion, in particular regions with rapid change between regions of very little variation. For the Lorenz system, we focus on recovering the system in the chaotic regime. For this reason we fix the parameters of the differential equation to lie in the region with large Lyapunov exponents and vary the initial conditions. The initial conditions are chosen from a uniform distribution,  $x_1, x_2 \sim U_{[-15,15]}$  and  $x_3 \sim U_{[10,40]}$ , which covers the strange attractor.

**3.1. Noise-Free Data.** The goal of the noise-free experiments is to examine the effect of increasing the polynomial degree  $p$  of the test functions to show that convergence to machine precision is realized in the limit of large  $p$  (i.e. convergence to within the accuracy tolerance of the ODE solver), as expected from Lemma 2. Indeed, Figure 3.1 shows that in the zero-noise case ( $\epsilon = 0$ ), WSINDy recovers the correct weight matrix  $\mathbf{w}^*$  to within the tolerance of the ODE solver (fixed at  $10^{-10}$ ) over a wide range of parameter values for each of the dynamical systems above. We find that accurate recovery occurs regardless of sparsity enforcement or regularization, and so we set  $\lambda = 0.001$  throughout, orders of magnitude below any of the true coefficients  $\mathbf{w}^*$ , and  $\gamma = 0$ . For the data-driven trial basis  $(f_j)_{j \in [J]}$ , we include all polynomials up to degree 5 in the state variables as well as  $\cos(ny_d)$ ,  $\sin(ny_d)$  for  $n = 1, 2$  and  $d \in [D]$ . In addition, we find that recovery occurs with the minimal number of basis functions  $K = J$  such that the Gram matrix  $\mathbf{G} = \mathbf{V}\Theta(\mathbf{y})$  is square. We use the uniform grid approach above with support  $L$  selected from the Fourier transform of  $\mathbf{y}$  and shift parameter  $s$  fixed to ensure that  $K = J$ .

**3.2. Small-Noise Regime.** We now turn to the case of low to moderate noise levels, examining a signal-to-noise ratio  $\sigma_{SNR}$  in the range  $[10^{-5}, 0.04]$ . In Figures 3.2 and 3.3 we observe another nice property of WSINDy, that the error in the coefficients scales with  $\sigma_{SNR}$ , in that the recovered coefficients  $\hat{\mathbf{w}}$  have approximately  $\log_{10}(10\sigma_{SNR}^{-1})$  significant digits.

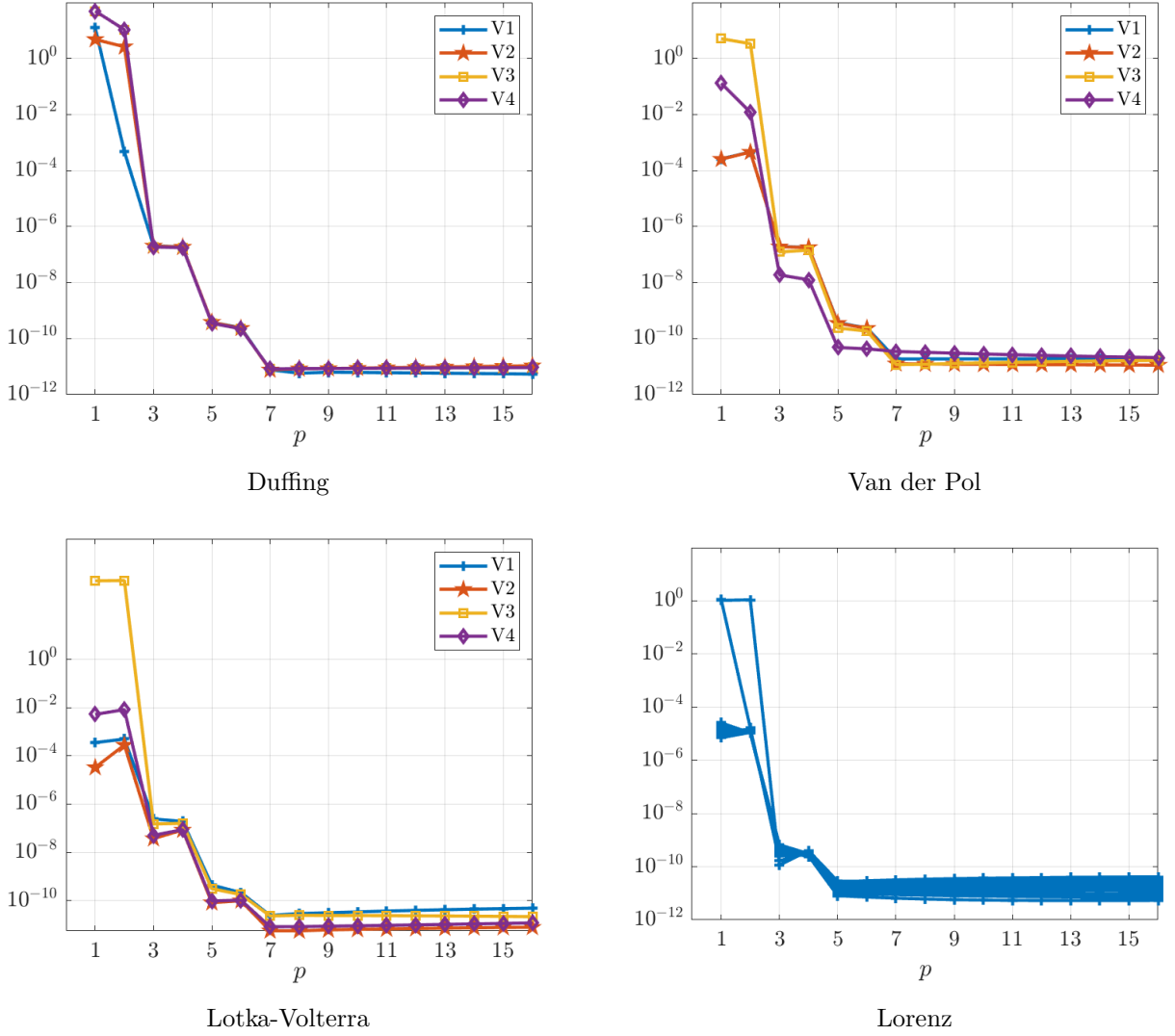


FIGURE 3.1. Noise-free data: plots of relative error  $\|\widehat{\mathbf{w}} - \mathbf{w}^*\|_2 / \|\mathbf{w}^*\|_2$  vs.  $p$  when  $\epsilon = 0$  using WSINDy\_UG. For each system, a range of parameter values is considered (see Table.1). In each case, the recovered coefficients  $\widehat{\mathbf{w}}$  rapidly converge to within the accuracy of the ODE solver ( $10^{-10}$ ) as  $p$  is increased. For the Duffing equation, Van der Pol oscillator and Lotka-Volterra system, convergence is shown for parameter sets V1-V4 spanning several orders of magnitude. For the Lorenz system, convergence is shown for 40 trajectories, each generated with initial conditions drawn randomly from a uniform distribution which covers the strange attractor.

We again use the uniform grid approach. We examine not only the polynomial degree  $p$  but the number of basis functions  $K$  used in recovery. To reiterate the arguments above, the magnitude of  $\phi'_k$  compared to  $\phi_k$  affects the distribution of the residual, so we define  $\rho := \|\phi'_k\|_\infty / \|\phi_k\|_\infty$  and define the degree  $p$  by fixing

	V1	V2	V3	V4	Notes
Duffing, $\beta$ :	0.005	0.08	1	100	$\mathbf{t} = 0 : 0.01 : 30$
Van der Pol, $\beta$ :	0.01	0.1	1	10	$\mathbf{t} = 0 : 0.01 : 30$
Lotka-Volterra, $\beta$ :	0.05	0.1	1	10	$\mathbf{t} = 0 : 0.01 : 30$
Lorenz	-	-	-	-	$\mathbf{x}(0) \sim U_{[-15,15]^2 \times [10,40]}$ , $\mathbf{t} = (0.001 : 0.001 : 10)$

TABLE 1. Specifications for parameters used in illustrating simulations in Figure 3.1.

$\rho$  and then calculating  $p$ . In this way, increasing  $\rho$  corresponds to increasing  $p$ . We look at  $\rho \in [1, 5]$  which corresponds roughly to  $p \in [4, 100]$ . This together with the spacing parameter  $s$  determines the test function basis. We enforce that two neighboring basis functions  $\phi_k$  and  $\phi_{k+1}$  intersect at a height of  $s$ , so that with  $s = 1$ , the two functions perfectly overlap, and with  $s = 0$  their supports are disjoint. In this way, larger  $s$  corresponds to higher  $K$ . We examine  $s \in (0, 1)$ . For  $s = 0.5$  (featured in both Figures) we note that as  $\rho$  is varied from 1 to 5, the number of basis functions  $K$  ranges from 21 to 105, or  $K = J$  to  $K = 5J$ . In each case we set the sparsity and regularization parameters to  $\lambda = \frac{1}{4} \min_{\mathbf{w}^* \neq 0} |\mathbf{w}^*|$  and  $\gamma = 0$  and use a trial basis  $(f_j)_{j \in [J]}$  consisting of all polynomials up to degree 5 in the state variables.

We simulated 200 instantiations of noise for the Duffing equation and Van der Pol oscillator and for each noisy trajectory examined a range of the parameter values  $s$  and  $\rho$ . As one might expect from the noise-free case above, increasing  $\rho$  leads monotonically to better recovery. In addition, increasing  $s$  also leads to better recovery. The mean and standard deviation of the coefficient error  $\|\widehat{\mathbf{w}} - \mathbf{w}^*\|_2 / \|\mathbf{w}^*\|_2$  are also pictured, along with sample trajectories from the resulting data-driven dynamical systems, denoted by  $\mathbf{x}_{dd}$ .

**3.3. Large-Noise Regime.** Figures 3.4 to 3.7 show that Strategy 2 (non-uniform grid) can be employed to discover the dynamics in the large noise regime. The signal to noise ratio is  $\sigma_{SNR} = 0.1$  for the Duffing, Van der Pol and Lorenz equations, and  $\sigma_{SNR} = 0.05$  for Lotka-Volterra. In each case we set the weak differentiation parameters to  $p = 2$  and  $s = 16$  and the width-at-half-max to  $r_{whm} = 30$  timepoints. For the 2D systems, we use  $K = 6J = 126$  test basis functions, while for the Lorenz equation  $K = 4J = 224$  were used. In each case the correct terms were identified with relative  $\ell_2$  coefficient error less than  $10^{-2}$ , indicating approximately two significant digits. We plot the noisy data  $\mathbf{y}$ , the true data  $\mathbf{x}$  and the simulated data-driven dynamical systems  $\mathbf{x}_{dd}$  in dynamo view and phase space to exemplify the separation of scales and the severity of the corruption from noise. We extend  $\mathbf{x}_{dd}$  by 50% to show that the data-driven system captures the expected limiting behavior. Unless otherwise specified, we set the sparsity and regularization parameters to  $\lambda = \frac{1}{4} \min_{\mathbf{w}^* \neq 0} |\mathbf{w}^*|$  and  $\gamma = 0$  and use a trial basis  $(f_j)_{j \in [J]}$  consisting of all polynomials up to degree 5 in the state variables.

For the Duffing equation (Figure 3.4), the data-driven trajectory  $\mathbf{x}_{dd}$  diverges slightly from the true data as the system relaxes to equilibrium but is qualitatively correct. The recovered Van der Pol oscillator (Figure 3.5) identifies the correct limit cycle but the dominant timescale of  $\mathbf{x}_{dd}$  is slightly shorter than the true data

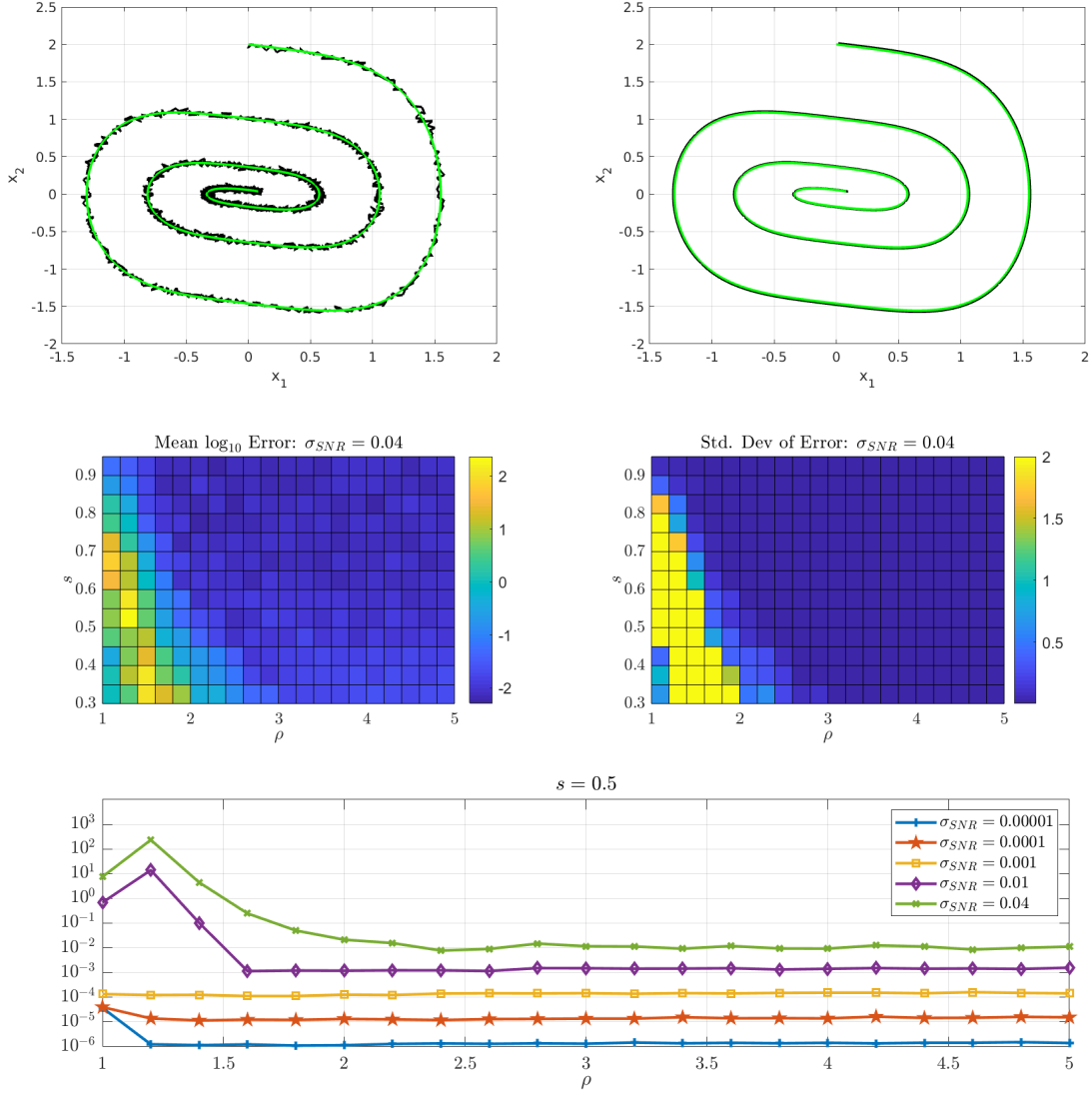


FIGURE 3.2. Low-noise regime: dynamic recovery of the Duffing equation with parameters  $\mu = 0.2, \alpha = 0.05, \beta = 1$ . Top row: example trajectory  $\mathbf{y}$  (left) and learned dynamics  $\mathbf{x}_{dd}$  (right) both plotted over true data  $\mathbf{x}$ . Here,  $\sigma_{SNR} = 0.04, \rho = 5, s = 0.5$  and the coefficient error is  $E := \|\widehat{\mathbf{w}} - \mathbf{w}^*\|_2 / \|\mathbf{w}^*\|_2 = 0.0009$ . Middle row: heat map of the  $\log_{10}$  average error  $E$  (left) and standard deviation (right) over 200 noisy trajectories with  $\sigma_{SNR} = 0.04$  with increasing  $\rho$  along the  $x$ -axis and increasing  $s$  along the  $y$ -axis. Bottom: decreasing error trend for fixed  $s = 0.5$  for various  $\sigma_{SNR}$ . For each  $\sigma_{SNR}$  the expected error falls roughly an order of magnitude below the  $\sigma_{SNR}$  as  $\rho$  increases.

$\mathbf{x}$ . For this reason  $\mathbf{x}_{dd}$  slowly diverges pointwise over time but does not stray from the relevant regions of phase space. This reflects that more accurate measurements are needed to recover systems with abrupt changes. The recovered Lotka-Volterra trajectory (Figure 3.6) is nearly indistinguishable from the true data,

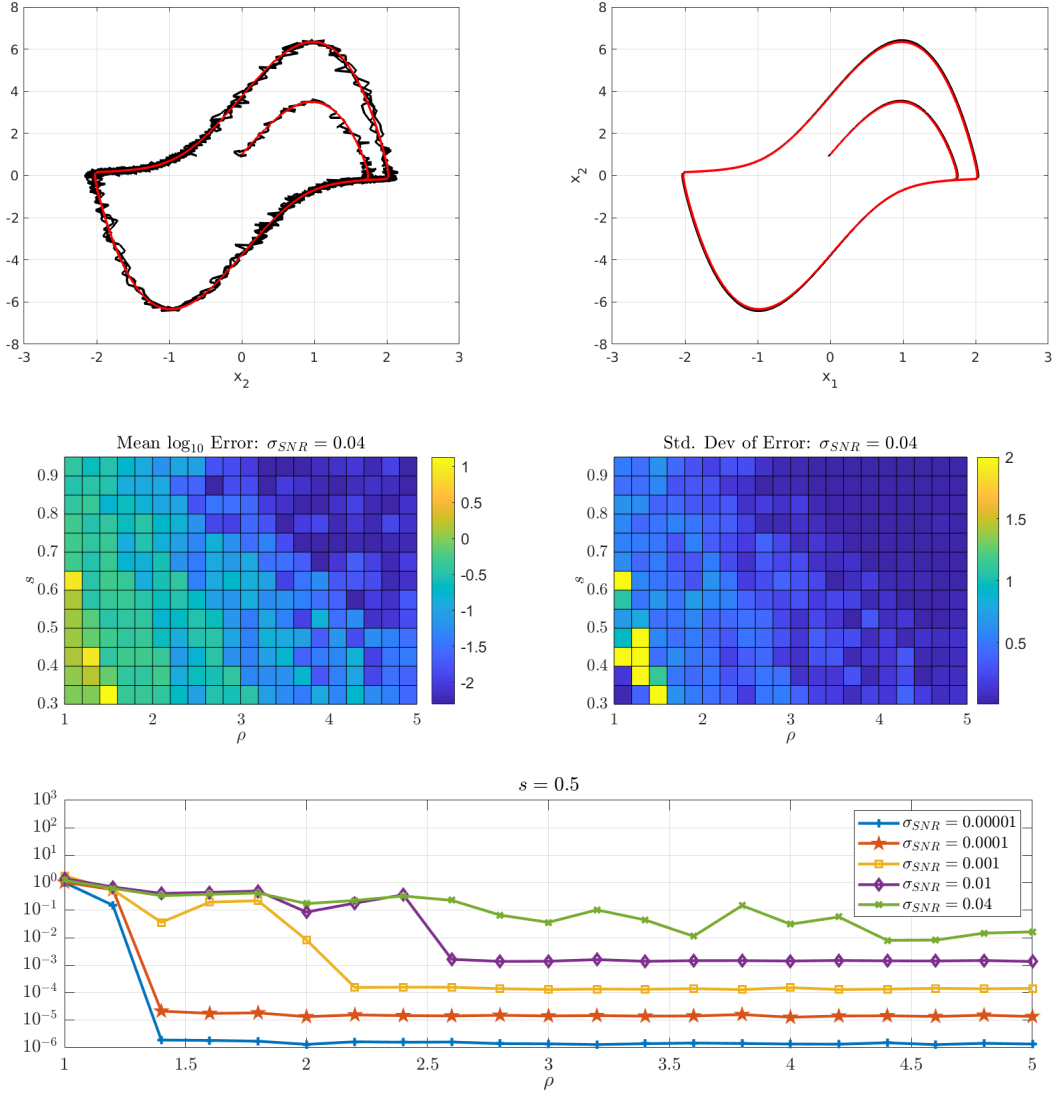


FIGURE 3.3. Low-noise regime: dynamic recovery of the Van der Pol oscillator with parameter  $\mu = 4$ . Top row: example trajectory  $\mathbf{y}$  (left) and learned dynamics  $\mathbf{x}_{dd}$  (right) both plotted over true data  $\mathbf{x}$ . Here  $\sigma_{SNR} = 0.04$ ,  $\rho = 5$ ,  $s = 0.5$  and an error of  $E := \|\widehat{\mathbf{w}} - \mathbf{w}^*\|_2 / \|\mathbf{w}^*\|_2 = 0.0026$ . Middle row: color plot of  $\log_{10}$  of the average error  $E$  (left) and standard deviation of the error  $E$  (right) over 200 noisy trajectories with  $\sigma_{SNR} = 0.04$  with increasing  $\rho$  along the  $x$ -axis and increasing  $s$  along the  $y$ -axis. Bottom: decreasing error trend for fixed  $s = 0.5$  for various  $\sigma_{SNR}$ . As with the Duffing equation in Figure 3.2, for each  $\sigma_{SNR}$  the expected error falls roughly an order of magnitude below the  $\sigma_{SNR}$  as  $\rho$  increases, however the expected accuracy begins to break down for larger  $\sigma_{SNR}$ , motivating the use of WSINDy\_AG for large noise.



but we note that here regularization was used ( $\gamma = 0.01$ ), as the system was nearly singular, and the columns of  $\Theta(\mathbf{y})$  were normalized using the 2-norm. For the Lorenz attractor (Figure 3.7), the recovered trajectory remains close to the true trajectory up until around  $t = 3$ , after which the two diverge as is expected from chaotic dynamics. Nevertheless the Lorenz attractor is captured.

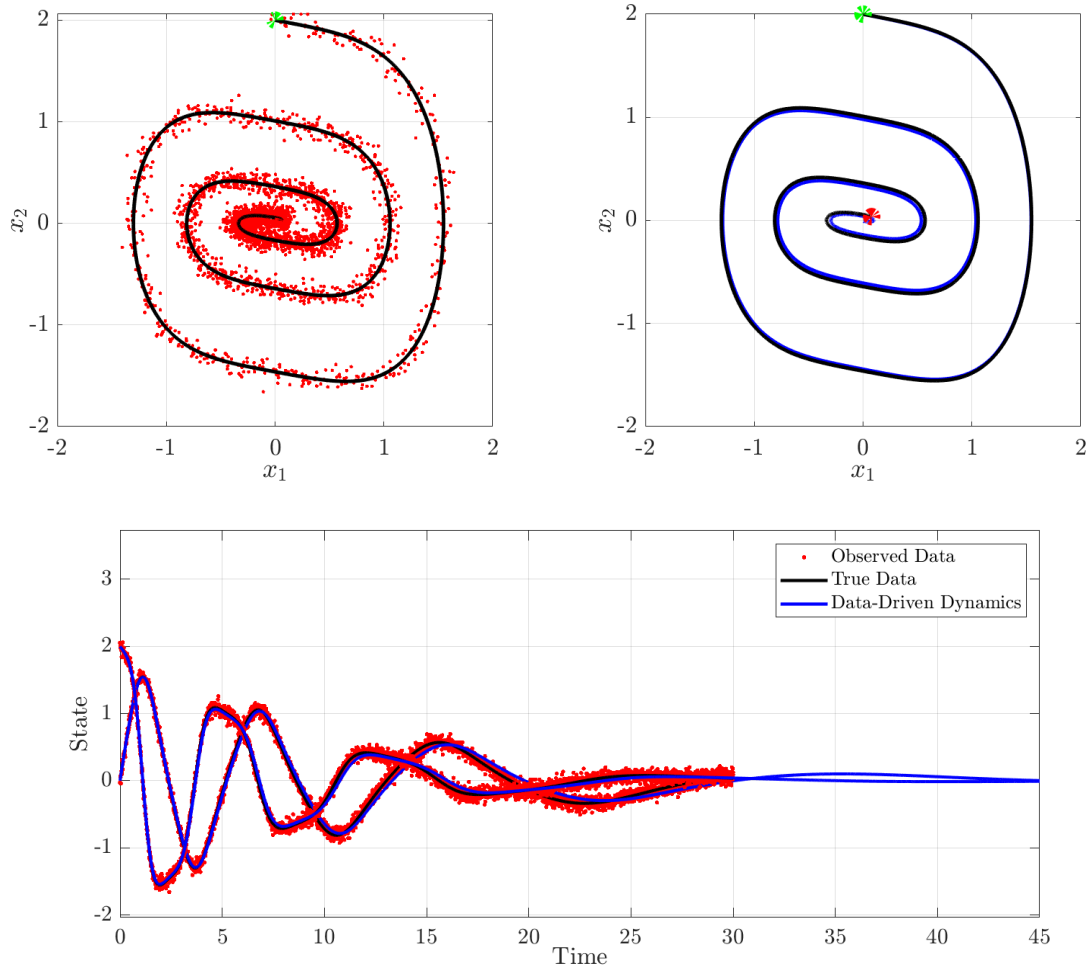


FIGURE 3.4. Large-noise regime: Duffing Equation, same parameters as in Figure 3.2. Accurate recovery of the stable spiral with  $\sigma_{SNR} = 0.1$ . All correct terms were identified with an error in the weights of  $\|\hat{\mathbf{w}} - \mathbf{w}^*\|_2 / \|\mathbf{w}^*\|_2 = 0.007$  and  $\|\mathbf{x}_{dd} - \mathbf{x}\|_2 / \|\mathbf{x}\|_2 = 0.097$ . The number of basis functions used was  $K = 6J = 126$  and the width-at-half-max parameter was set to  $r_{whm} = 30$  time-points, resulting in  $p = 10$ .

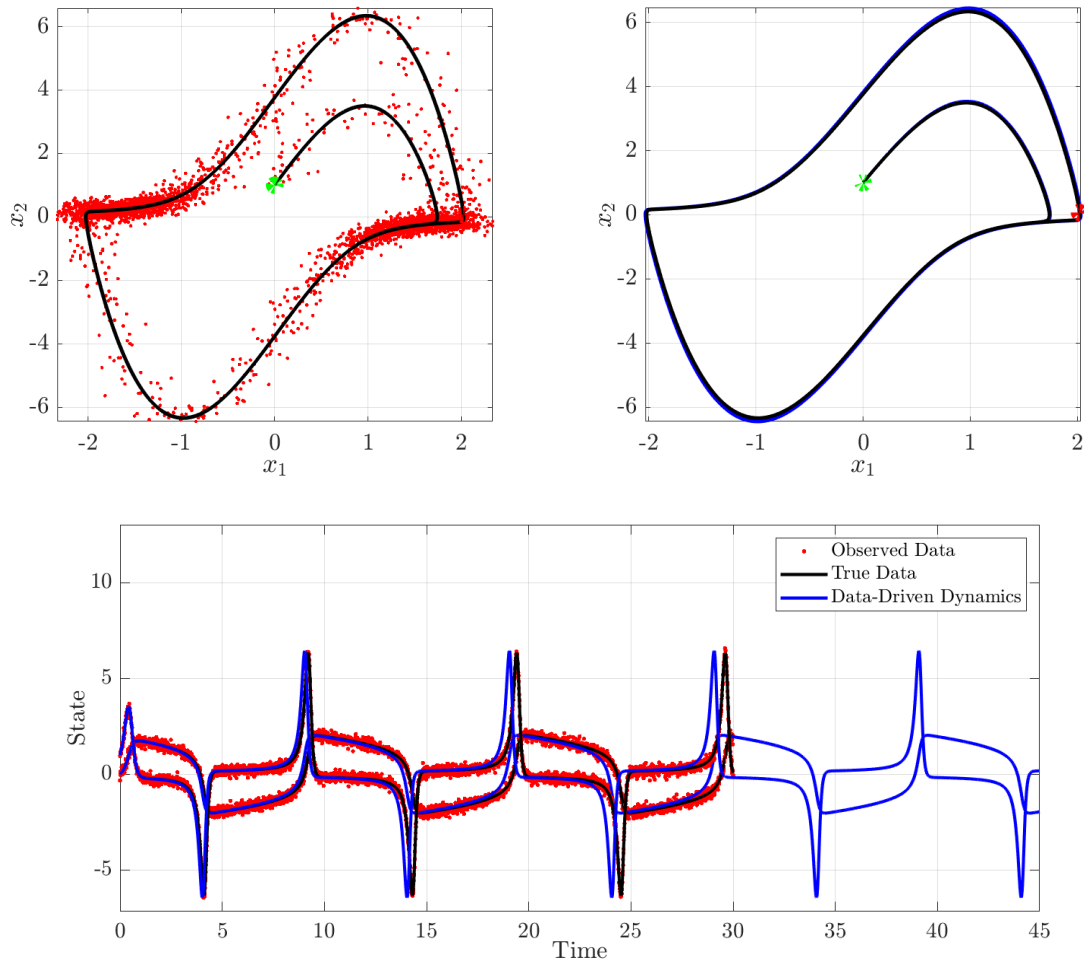


FIGURE 3.5. Large-noise regime: Van der Pol oscillator, same parameters as in Figure 3.3. Accurate recovery of the limit cycle for  $\sigma_{SNR} = 0.1$ . All correct terms were identified with an error in the weights of  $\|\hat{\mathbf{w}} - \mathbf{w}^*\|_2 / \|\mathbf{w}^*\|_2 = 0.008$  and  $\|\mathbf{x}_{dd} - \mathbf{x}\|_2 / \|\mathbf{x}\|_2 = 0.56$ . The number of basis functions used was  $K = 6J = 126$  and the width-at-half-max parameter was set to  $r_{whm} = 30$  timepoints, resulting in  $p = 10$ . Here we see that the data-driven system  $\mathbf{x}_{dd}$  traverses the limit cycle with a slightly shorter period, resulting in a growing pointwise error between the  $\mathbf{x}_{dd}$  and the true state  $\mathbf{x}$ .

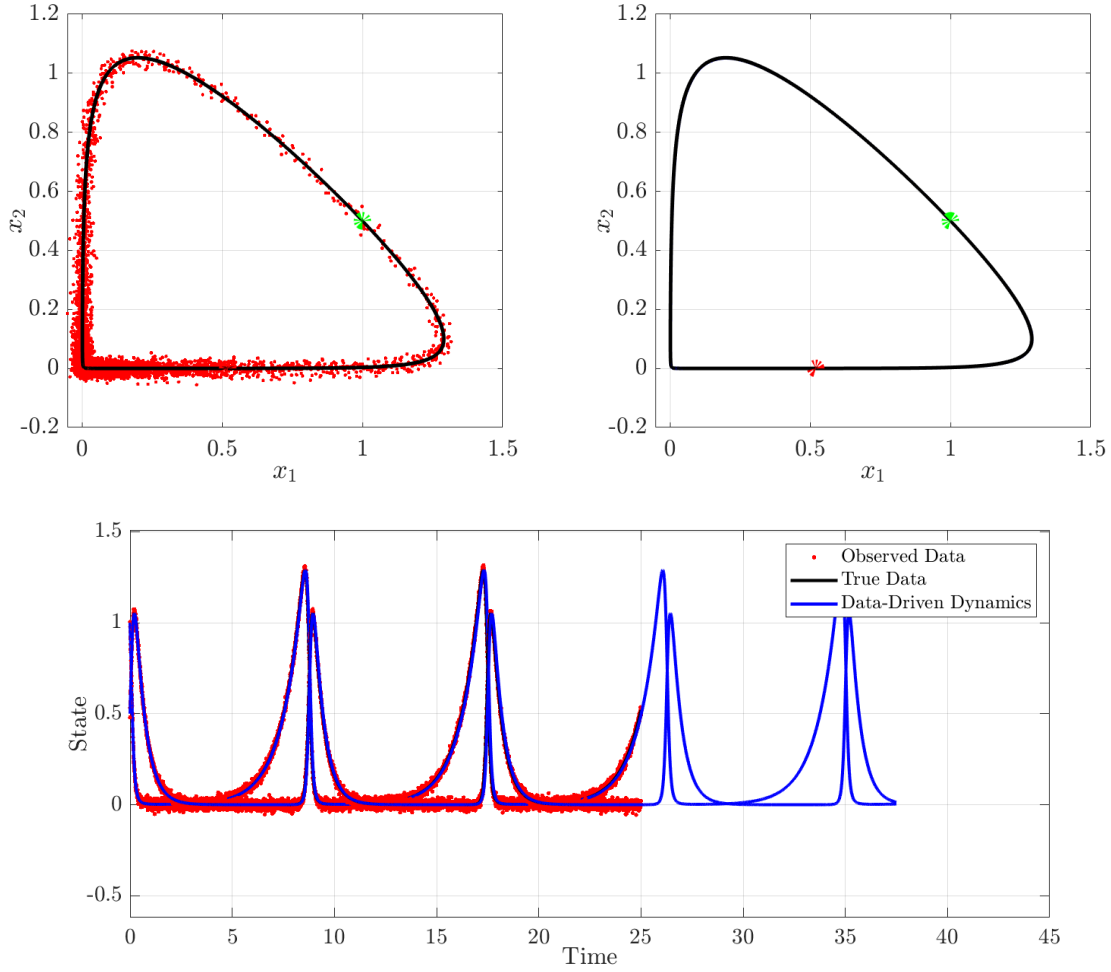


FIGURE 3.6. Large-noise regime: Lotka-Volterra system with  $\alpha = 1, \beta = 10$ . Accurate recovery of the limit cycle for  $\sigma_{SNR} = 0.05$ . All correct terms were identified with an error in the weights of  $\|\widehat{\mathbf{w}} - \mathbf{w}^*\|_2 / \|\mathbf{w}^*\|_2 = 0.0032$  and  $\|\mathbf{x}_{dd} - \mathbf{x}\|_2 / \|\mathbf{x}\|_2 = 0.065$ . The number of basis functions used was  $K = 6J = 126$  and the width-at-half-max parameter was set to  $r_{whm} = 30$  timepoints, resulting in  $p = 10$ . The data-driven system  $\mathbf{x}_{dd}$  accurately captures the limit cycle and traverses at the same speed as the true data  $\mathbf{x}$ . Here we set  $\gamma = 0.01$  and normalized the columns of  $\Theta(\mathbf{y})$  using the 2-norm as the original system is nearly linearly dependent.

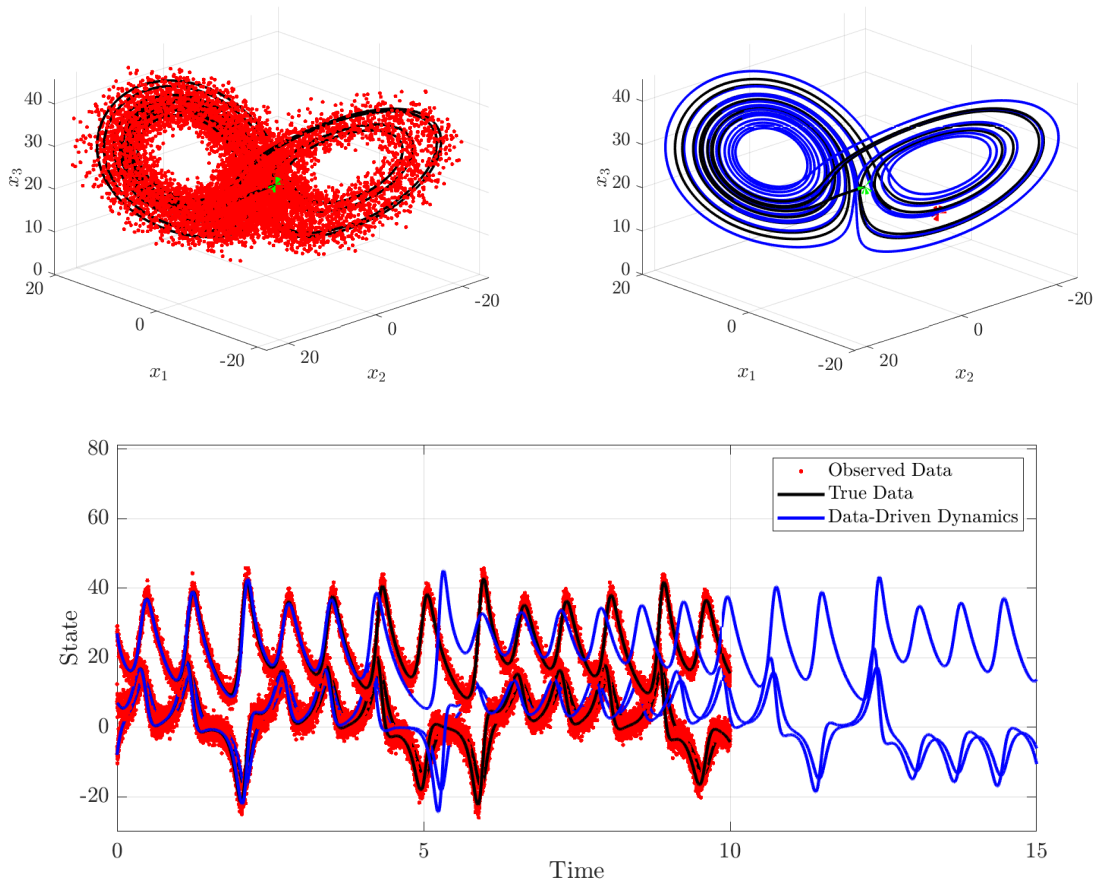


FIGURE 3.7. Large-noise regime: Lorenz system with  $\mathbf{x}_0 = [-8 \ 7 \ 27]^T$ . Accurate recovery of the strange attractor for  $\sigma_{SNR} = 0.1$ . All correct terms were identified with an error in the weights of  $\|\hat{\mathbf{w}} - \mathbf{w}^*\|_2 / \|\mathbf{w}^*\|_2 = 0.0091$ . Since the system is chaotic it does not make sense to measure the pointwise error between the data-driven trajectory  $\mathbf{x}_{dd}$  and the true data  $\mathbf{x}$  for large times, but using data up until  $t = 3$  (first 3000 timepoints) we can report a reasonable pointwise agreement of  $\|\mathbf{x}_{dd} - \mathbf{x}\|_2 / \|\mathbf{x}\|_2 = 0.047$ . The number of basis functions used was  $K = 4J = 224$  and the width-at-half-max parameter was set to  $r_{whm} = 30$  timepoints, resulting in  $p = 10$ .

#### 4. CONCLUDING REMARKS

We have developed and investigated a data-driven model selection algorithm based on the weak formulation of differential equations. The algorithm utilizes the reformulation of the model selection problem as a sparse regression problem for the weights  $\mathbf{w}^*$  of a candidate function basis  $(f_j)_{j \in [J]}$  introduced in [14] and generalized in [4] as the SINDy algorithm. Our Weak SINDy algorithm (WSINDy) can be seen as a generalization of the sparse recovery scheme using integral terms found in [12], where dynamics were recovered from the integral equation.

A natural line of inquiry is to consider how WSINDy compares with conventional SINDy. There are several notable advantages of WSINDy; in particular, by considering a weak form of the equations, WSINDy completely avoids any evaluation of the pointwise derivatives which cause significant accuracy problems in conventional SINDy. While our work here is not the first to consider integrals of the differential equation,<sup>1</sup> WSINDy is a much more general methodology with natural extensions that draw upon the rich and well-established finite element literature. Furthermore, the integration operation itself is a linear operator, allowing estimation of covariance structures, which allow computation of solutions in a weighted least squares framework (which is substantially more accurate than ordinary least squares).

In our future work, we also plan to pursue direct computational comparisons with conventional SINDy to illustrate concrete benefits of the WSINDy framework. For example, our preliminary efforts (not reported here) suggest that the relationship between noise and coefficient error appears to be more predictable in WSINDy than conventional SINDy. As Figures 3.2 and 3.3 suggest, WSINDy appears to scale continuously with the SNR and without the use of noise filtering, a trend which simply cannot be expected from pointwise derivative approximations. Our preliminary efforts also suggest that the linear systems are smaller, requiring fewer data points, but more overall floating point operations. Clearly a more complete analysis is required to fully understand the tradeoffs between WSINDy and SINDy.

Lastly, the most obvious extensions lie in generalizing the WSINDy method for spatiotemporal datasets and problems with multiple timescales. WSINDy as presented here in the context of ODEs is an exciting proof of concept, with natural extensions to spatiotemporal and multiresolution settings building upon the extensive results in numerical and functional analysis for weak and variational formulations of physical problems.

## 5. ACKNOWLEDGEMENTS

This research was supported in part by the NSF/NIH Joint DMS/NIGMS Mathematical Biology Initiative grant R01GM126559 and in part by the NSF Computing and Communications Foundations Division grant CCF-1815983.

## REFERENCES

- [1] H. Akaike. A new look at the statistical model identification. *IEEE Transactions on Automatic Control*, 19(6):716–723, December 1974.
- [2] Hirotugu Akaike. On entropy maximization principle. In P. R. Krishnaiah, editor, *Applications of Statistics*, pages 27–41. North Holland, Amsterdam, Netherlands, 1977.
- [3] D. M. Bortz and P. W. Nelson. Model Selection and Mixed-Effects Modeling of HIV Infection Dynamics. *Bulletin of Mathematical Biology*, 68(8):2005–2025, November 2006.
- [4] Steven L Brunton, Joshua L Proctor, and J Nathan Kutz. Discovering governing equations from data by sparse identification of nonlinear dynamical systems. *Proceedings of the national academy of sciences*, 113(15):3932–3937, 2016.
- [5] Germund Dahlquist and Ake Björck. *Numerical Methods in Scientific Computing: Volume 1*, volume 103. Siam, 2008.
- [6] Sung Ha Kang, Wenjing Liao, and Yingjie Liu. Ident: Identifying differential equations with numerical time evolution. *arXiv preprint arXiv:1904.03538*, 2019.

---

<sup>1</sup>To the best of the author’s knowledge [12] was the first (and only other) such effort.

- [7] Rachel Keller and Qiang Du. Discovery of dynamics using linear multistep methods. *arXiv preprint arXiv:1912.12728*, 2019.
- [8] John H. Lagergren, John T. Nardini, G. Michael Lavigne, Erica M. Rutter, and Kevin B. Flores. Learning partial differential equations for biological transport models from noisy spatio-temporal data. *Proc. R. Soc. A.*, 476(2234):20190800, February 2020.
- [9] Gabriele Lillacci and Mustafa Khammash. Parameter Estimation and Model Selection in Computational Biology. *PLoS Comput Biol*, 6(3):e1000696, March 2010.
- [10] Maziar Raissi, Paris Perdikaris, and George Em Karniadakis. Machine learning of linear differential equations using Gaussian processes. *Journal of Computational Physics*, 348:683–693, 2017.
- [11] Samuel H Rudy, J Nathan Kutz, and Steven L Brunton. Deep learning of dynamics and signal-noise decomposition with time-stepping constraints. *Journal of Computational Physics*, 396:483–506, 2019.
- [12] Hayden Schaeffer and Scott G McCalla. Sparse model selection via integral terms. *Physical Review E*, 96(2):023302, 2017.
- [13] Tina Toni, David Welch, Natalja Strelkowa, Andreas Ipsen, and Michael P.H Stumpf. Approximate Bayesian computation scheme for parameter inference and model selection in dynamical systems. *J. R. Soc. Interface.*, 6(31):187–202, February 2009.
- [14] Wen-Xu Wang, Rui Yang, Ying-Cheng Lai, Vassilios Kovanis, and Celso Grebogi. Predicting catastrophes in nonlinear dynamical systems by compressive sensing. *Physical review letters*, 106(15):154101, 2011.
- [15] David J. Warne, Ruth E. Baker, and Matthew J. Simpson. Using Experimental Data and Information Criteria to Guide Model Selection for Reaction–Diffusion Problems in Mathematical Biology. *Bull Math Biol*, 81(6):1760–1804, June 2019.
- [16] Hulin Wu and Lang Wu. Identification of significant host factors for HIV dynamics modelled by non-linear mixed-effects models. *Statist. Med.*, 21(5):753–771, March 2002.
- [17] Linan Zhang and Hayden Schaeffer. On the convergence of the SINDy algorithm. *Multiscale Modeling & Simulation*, 17(3):948–972, 2019.
- [18] Sheng Zhang and Guang Lin. Robust data-driven discovery of governing physical laws with error bars. *Proceedings of the Royal Society A: Mathematical, Physical and Engineering Sciences*, 474(2217):20180305, 2018.
- [19] Sheng Zhang and Guang Lin. Robust subsampling-based sparse Bayesian inference to tackle four challenges (large noise, outliers, data integration, and extrapolation) in the discovery of physical laws from. *arXiv preprint arXiv:1907.07788*, 2019.

*E-mail address:* daniel.messenger@colorado.edu, dmbortz@colorado.edu, Department of Applied Mathematics, University of Colorado, Boulder, CO 80309-0526, USA.